

# Is Exchangeability better than I.I.D to handle Data Distribution Shifts while Pooling Data for Data-scarce Medical image segmentation?

Ayush Roy<sup>1</sup> Samin Enam<sup>1</sup> Jun Xia<sup>1</sup>  
Won Hwa Kim<sup>2</sup> Vishnu Suresh Lokhande<sup>1</sup>

<sup>1</sup>University at Buffalo, SUNY <sup>2</sup>Pohang University of Science and Technology

{aroy25, vishnulo, saminena, junxia}@buffalo.edu {wonhwa}@postech.ac.kr

## Abstract

*Data scarcity is a major challenge in medical imaging, particularly for deep learning models. While data pooling (combining datasets from multiple sources) and data addition (adding more data from a new dataset) have been shown to enhance model performance, they are not without complications. Specifically, increasing the size of the training dataset through pooling or addition can induce distributional shifts, negatively affecting downstream model performance, a phenomenon known as the “Data Addition Dilemma”. While the traditional i.i.d. assumption may not hold in multi-source contexts, assuming exchangeability across datasets provides a more practical framework for data pooling. In this work, we investigate medical image segmentation under these conditions, drawing insights from causal frameworks to propose a method for controlling foreground-background feature discrepancies across all layers of deep networks. This approach improves feature representations, which are crucial in data-addition scenarios. Our method achieves state-of-the-art segmentation performance on histopathology and ultrasound images across five datasets, including a novel ultrasound dataset that we have curated and contributed. Qualitative results demonstrate more refined and accurate segmentation maps compared to prominent baselines across three model architectures. The code will be available on Github.*

## 1. Introduction

Medical imaging datasets often suffer from limited sample sizes due to budget constraints and strict study criteria, including genetic risk factors. This scarcity is further compounded by the lack of diagnostic labels, posing challenges for deep learning models that rely on supervised learning. Small datasets amplify the risk of models learning spurious correlations [67], while distributional disparities hinder generalization to real-world clinical settings. In addition to that, smaller number of training samples lead to data

memorization, data interpolation, and high variance models [41, 49, 53, 77], all causing poor generalization. Though deep learning advancements show promise, issues of data quality and distribution mismatches remain significant barriers [47]. Semi-supervised learning and data augmentation provide partial solutions with varying effectiveness [12]. Pooling data from multiple sites, combined with techniques like covariate matching and meta-analysis, has improved model robustness and generalization [42].

**Limitations of Data Augmentation in Medical Imaging.** Data augmentation techniques, including rotations, flips, and crops are widely employed to improve model robustness by generating synthetic training samples [9]. However, in medical imaging, these methods often introduce clinically unrealistic artifacts. For example, flipping or cropping brain images can disrupt inherent anatomical asymmetries critical for diagnosis, leading to misleading predictions [3]. Furthermore, such techniques frequently fail to preserve realistic variations in object boundaries (e.g., tumor margins) and spatial relationships between structures, significantly limiting their utility in tasks like semantic segmentation [25, 51].

**Alternatives of Augmentation: Data Pooling and Data Addition.** Given the limitations of data augmentation, two prominent alternatives emerge: data pooling and data addition. Data pooling aggregates datasets from multiple institutions to enhance statistical power and diversity. However, integration is hindered by distributional shifts (e.g., scanner variations, population differences) and non-i.i.d. (non-independent and identically distributed) data structures, where sources exhibit divergent feature distributions and dependencies as shown in Fig. 1 (b). To address this, harmonization algorithms (e.g., [48]) are required to align datasets before pooling [42]. A more practical alternative is data addition, which incrementally integrates new data into a pre-trained model while retaining prior knowledge. Unlike pooling, which is model-agnostic, data ad-

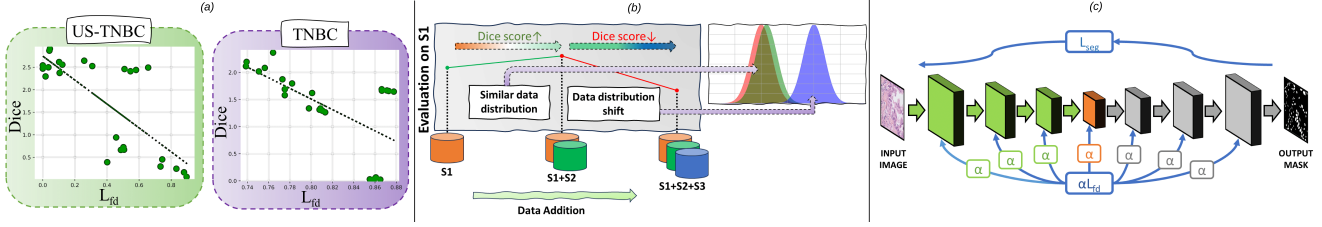


Figure 1. (a) **Strong correlation between Dice and  $\mathcal{L}_{fd}$  (foreground-background feature discrepancy loss)**. Strong correlation observed in both NucleiSegNet decoder layers and CMUNet encoder layers for ultrasound and histopathology images. (b) **Impact of Data Distribution Shift on Model Performance**. Dice score on the test dataset of S1 improves when the training data of S2 is added along with the training data of S1, due to their similar data distributions. This is expected as a pooled dataset having more training data will lead to better performance. However, performance drops upon adding S3, which exhibits a distribution shift relative to S1 and S2, consistent with observations in [62]. (c) **Proposed  $\mathcal{L}_{fd}$  applied to all the U-Net layers**. Green blocks represent the features from Encoder layers, grey blocks are the Decoder layer features, and the orange block is the Bottleneck layer feature. All of them represent the mediator variable ( $Z$ ) which is optimized by  $\mathcal{L}_{fd}$ . Each layer uses feature discrepancy loss  $\mathcal{L}_{fd}$ , with a unique learnable parameter  $\alpha$ .

dition necessitates adaptation strategies, either modifying the new data or fine-tuning the model, to reconcile distribution mismatches. Recent studies reveal a critical challenge termed the “data addition dilemma” [62], where expanding training data can paradoxically degrade performance due to unresolved distribution shifts. This underscores the need for robust strategies to balance incremental learning with stability.

#### Causality-Driven Approaches.

To address the challenges of distribution shifts and annotation biases in medical imaging (as outlined in Sections 1–2), causality-driven frameworks [10] are ideal for our selected task of segmentation in breast cancer and Alzheimer’s Disease (AD). Breast cancer, the most prevalent cancer in women, causes over 14,000 annual deaths in Algeria alone [1, 38]. Early detection relies on

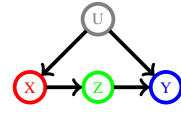


Figure 3. Causal graph linking input  $X$ , mediator  $Z$ , label  $Y$ , and unobserved confounders  $U$ .

imaging modalities like mammography and histopathology to identify lesions (e.g., nodules [21], microcalcifications [70]), while AD diagnosis hinges on quantifying tau protein aggregates in brain tissue. Current methods for lesion or plaque quantification are labor-intensive and error-prone, necessitating automated solutions.

However, traditional segmentation models often fail to generalize due to unobserved confounders (e.g., scanner artifacts, anatomical variability) that corrupt the causal relationship between images  $X$  and annotations  $Y$ . Causal inference offers a principled framework for modeling challenges in medical imaging [4, 52, 59]. As illustrated in Fig. 3, confounders  $U$  (e.g., imaging protocols, patient demographics) influence both  $X$  and  $Y$ , introducing spurious correlations. To address this, we adopt frontdoor adjustment [52], using a mediator  $Z$ , the foreground, background feature discrepancy, to disentangle causal effects. Our Feature Discrepancy Loss  $\mathcal{L}_{fd}$  operationalizes this adjustment by enhancing  $Z$ ’s robustness to  $U$ , minimizing its distributional shifts across datasets. This ensures that  $Y$  depends causally on  $X$ , not on confounders. Aligned with causal diagrams [10], this addresses the “data addition dilemma” (Sec. 2) by stabilizing features during incremental learning. Linking  $\mathcal{L}_{fd}$  to causal theory bridges high-level concepts (confounders, frontdoor criteria) with model design. Selection bias from noise in  $X$  (e.g., artifacts) that distorts the causal path  $X \rightarrow Y$  [10] is mitigated, while label noise in  $Y$  (e.g., annotator subjectivity) remains a separate challenge handled via label correction methods. This enables models to generalize in real-world clinical settings where unobserved biases are common.

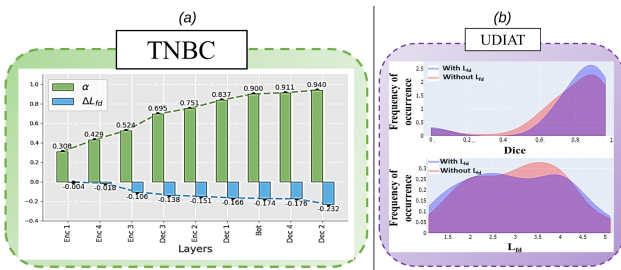


Figure 2. (a)  $\alpha$  (layer-wise weights) vs  $\mathcal{L}_{fd}$  (feature discrepancy loss) for NucleiSegNet layers (TNBC) shows a similar trend across all models and datasets. (b) Illustration of right and left shifts in the test sample distribution for Dice scores and  $\mathcal{L}_{fd}$  after applying  $\mathcal{L}_{fd}$  (orange curve) for CMUNet (UDIAT), with a similar trend across datasets. Refined activation maps justify this improvement in Dice scores (see Figure 5, Dec 4 and Bot) after penalizing foreground-background discrepancy with  $\mathcal{L}_{fd}$ .

**Contributions.** This paper focuses on the segmentation task in medical imaging, a field that *still* presents significant challenges in accurately delineating complex anatomical structures and pathologies [45]. Moreover, we leverage smaller models like UNet for our analysis. They remain sufficient in medical imaging due to their ability to accurately

segment with limited data and minimal reliance on prompts or extensive fine-tuning [2, 78]. Our contributions stem from the observation that the Dice Score, a commonly used metric for evaluating segmentation quality, correlates with the discrepancy between foreground and background features in the intermediate representations generated by neural networks. This observation holds true across ultrasound and histopathology images (Fig 1 (a)), prompting the question: *Can controlling for foreground-background feature discrepancy improve the quality of these representations and, consequently, the Dice Score?* We show that it does. Specifically, we propose: **(a)** a feature discrepancy loss to enhance feature distinction, reducing over- and under-segmentation in homogeneous pixel distributions; **(b)** a theoretical bound showing that the negative logarithm of the Dice coefficient serves as a lower bound for the feature discrepancy loss, ensuring improved Dice scores when optimizing for this loss; **(c)** a theoretical proof demonstrating the fact that the proposed feature discrepancy loss constrains the magnitude of the UNet layer weights, preventing the formation of a high-variance model prone to data memorization, a common issue in medical imaging datasets prone to limited samples; **(d)** introduction of a new ultrasound breast cancer dataset focused on triple-negative breast cancer (TNBC); and **(e)** a causal approach to address dataset distribution shift when integrating data from multiple sources. We achieve better segmentation performance across five datasets and significantly improve the segmentation performance of three prominent architectures.

## 2. Related Works

Recent advances in deep learning have surpassed traditional segmentation methods like watersheds [7] and super-pixels [40], demonstrating high efficacy in medical image segmentation [15, 33, 34, 43, 55, 64]. While MCFNet [22] captures spatial information, it struggles with complex staining patterns. Multimodal approaches [16, 20, 56, 57, 68, 82] integrate spatial and textual data but face challenges with homogeneous pixel distributions in medical images.

Loss-based approaches like contrastive loss [11, 73], deep supervision [19], and entropy minimization [23] improve U-Net [55] segmentation by refining foreground and background representations. Entropy minimization and contrastive losses separate pixel-level class representations. Our method also uses foreground-background feature discrepancy but penalizes all U-Net layers. Deep supervision applies binary cross-entropy loss to decoder outputs without contrastive losses. Approaches like [26, 29] enhance class consistency and feature re-ranking, but none penalize feature discrepancy across all layers. Our work is the first to show that layer-wise foreground-background discrepancy improves U-Net [55] representations, addressing the “data addition dilemma” [62]. In addition to that, all the afore-

mentioned losses are based on the strong i.i.d. assumption, which does not hold true always, as discussed in Sections 1 and 5. *Furthermore, segmentation tasks involve assigning a label to each pixel (or region) in an image, resulting in a structured output with strong spatial dependencies among pixels or regions, unlike classification that assigns a single label to the entire image (treating each sample as an independent entity).* In segmentation, the data points (pixels or regions) within an image are not independent; their labels are often correlated due to spatial continuity and object boundaries. Therefore, the i.i.d. assumption is often violated, making exchangeability, a weaker and more realistic assumption, more appropriate.

SAM [35], though powerful, is unsuitable for medical images due to its reliance on prompts and inability to handle numerous objects of interest without guidance [46]. Large models like Transformers require extensive data, which is scarce in medical imaging [28], and fine-tuning pre-trained models can introduce modality biases [5, 36] and unobserved task-irrelevant confounders (U in Fig. 3)[80]. Furthermore, Transformer architectures like TransUNet [14] and SwinUNet [8] suffer from oversegmentation and are unable to determine the foreground structure accurately compared to their UNet counterparts [81] (see Supplementary Sec E) for a comparison of the transformer architectures with our method). These challenges explain why U-Net variants remain the most widely adopted segmentation models in medical imaging [2, 78].

## 3. Method

Causal diagrams formalize assumptions about data generation, improving model robustness and generalization to clinical data, which enhances diagnostic tools. Causal reasoning helps address data scarcity by analyzing cause-effect relationships. In our study of medical images ( $X$ ) and their corresponding segmentation ground truth ( $Y$ ), we explore the causal relationship between them. The relationship may be causal ( $X \rightarrow Y$ ), indicating  $Y$  depends on  $X$ , or anti-causal ( $Y \rightarrow X$ ), predicting the cause from the effect. The task is to estimate  $P(Y | X)$ . Manual segmentation is influenced by image content, resolution, contrast, and annotator understanding, thus suggesting a causal model,  $X \rightarrow Y$ .

**Axiom 1. (Modularity for  $X \rightarrow Y$ ):** *In the causal graph where  $X$  causes  $Y$ , intervening on  $X$  changes only the mechanism determining  $X$ , while the mechanism determining  $Y$  given  $X$  remains invariant.*

Axiom 1 indicates that  $P(X)$  offers minimal information compared to  $P(Y | X)$ , implying that data augmentation and semi-supervised learning techniques are theoretically inadequate for resolving the data scarcity issue. A model trained on image-derived annotations will mainly reproduce the manual annotation process instead of predicting a pre-imaging ground truth, like the ‘true’ anatomy. While efforts

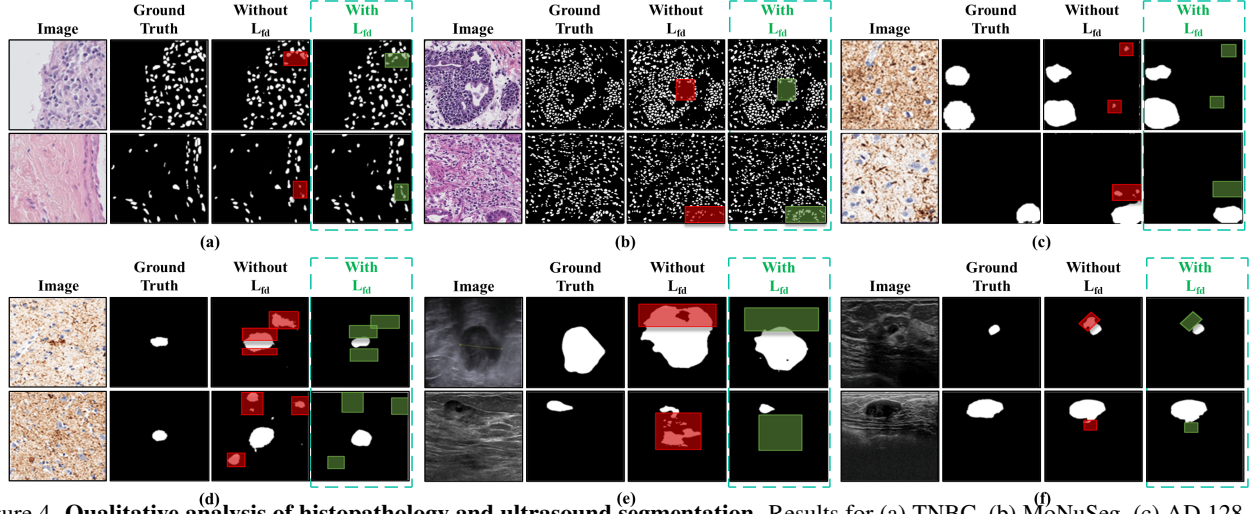


Figure 4. **Qualitative analysis of histopathology and ultrasound segmentation.** Results for (a) TNBC, (b) MoNuSeg, (c) AD 128, and (d) AD 256 datasets of NucleiSegNet, and for (e) US-TNBC and (f) UDIAT datasets of CMUNet, with (green) and without  $\mathcal{L}_{fd}$ . Red boxes highlight faulty segmentation without  $\mathcal{L}_{fd}$ , while green boxes show improvements with  $\mathcal{L}_{fd}$ .

to enhance data augmentation techniques for segmentation tasks continue [76], our approach emphasizes utilizing existing data to improve segmentation outcomes.

### 3.1. Handling Data Scarcity through Causal Mediation

In data-scarce scenarios, the effective utilization of available samples is crucial. One approach focuses on improving the performance of underperforming samples, aligning with the Rawlsian principle [44] of prioritizing the worst-off samples. While techniques like upweighting show promise, they are impractical here due to the challenge of estimat-

ing reliable probability distributions in medical imaging datasets. To address this, we introduce causal mediation by incorporating mediator  $Z$ , as depicted in Fig. 3. Derived from the image  $X$ ,  $Z$  serves as a differentiable proxy for  $Y$ , mediating the relationship to enhance performance.

**Proposition 1. (Mediation in Causal Prediction Model):** *Given a causal diagram  $X \rightarrow Y$ , introducing a mediator  $Z$  to create the structure  $X \rightarrow Z \rightarrow Y$ , and assuming a strong correlation between  $Y$  and  $Z$ , this results in*

- *Conditional Independence:*  $(X \perp Y) \mid Z$
- *Preserved Modularity:*  $P(X) \perp P(Y \mid X)$
- *Functional Relationship:*  $P(Y \mid X) = \int P(Y \mid Z)P(Z \mid X)$ .

The relationship shown in Proposition (1) indicates that  $P(Y \mid X)$  depends on  $P(Z \mid X)$ , as  $Z$  mediates  $X \rightarrow Y$ . This indicates that an accurate determination of  $P(Z \mid X)$  allows for precise estimation of  $P(Y \mid X)$ .

**Example 1.** Consider  $X \sim \mathcal{N}(0, 1)$ , where  $\mathcal{N}$  denotes the normal distribution. Define  $Z = aX + \epsilon_1$  and  $Y = bZ + \epsilon_2$ , where  $\epsilon_1 \sim \mathcal{N}(0, 1)$  and  $\epsilon_2 \sim \mathcal{N}(0, 1)$ , and  $a$  and  $b$  are constants. Under these definitions, we have the following conditional distributions:  $Z \mid X \sim \mathcal{N}(aX, 1)$ ,  $Y \mid Z \sim \mathcal{N}(bZ, 1)$ , and consequently  $Y \mid X \sim \mathcal{N}(abX, 1 + b^2)$ .

The example demonstrates that  $P(Y \mid X)$  is a function of  $P(Z \mid X)$ , as the mean of  $Y \mid X$  (represented as  $abX$ ) depends on the mean of  $Z \mid X$  (which is  $aX$ ). Moreover, conditional independence is preserved, as knowing  $X$  provides no further information about  $Y$  given  $Z$ .

### 3.2. Mediator as a Feature Discrepancy Measure

We now focus on identifying the appropriate mediator variable  $Z$ . From the previous section, we know that a good mediator  $Z$  should exhibit a strong correlation with  $Y$  and

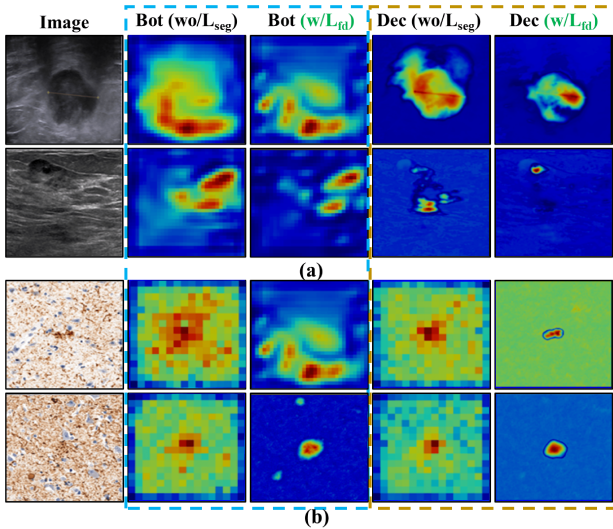


Figure 5. **Heatmaps with and without the use of  $\mathcal{L}_{fd}$ .** Heatmaps of the bottleneck layer (Bot) and the last decoder layer (Dec) of NucleiSegNet and CMUNet for AD and US-TNBC respectively. With  $\mathcal{L}_{fd}$  (green), the erroneous activation maps are reduced, leading to better-predicted segmentation masks.



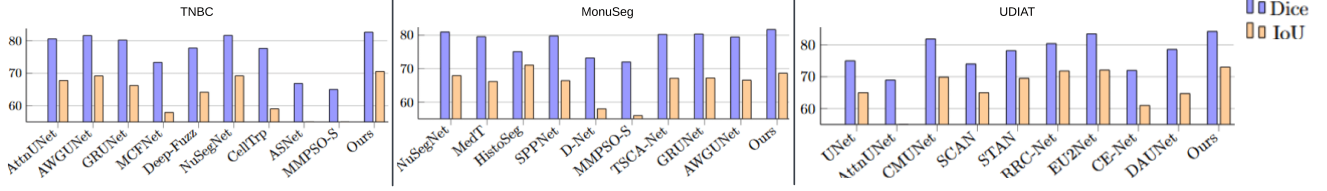


Figure 6. **Comparison of the proposed method with existing models for various datasets.** We compare our model with MedT [71], HistSeg [72], SPPNet [74], D-Net [30], MMPSO-S [33], TSCA-Net [24], GRUNet [56] and AWGUNet [57] for MoNuSeg [37], AWGUNet [57], GRUNet [56], MCFNet [22], Deep-Fuzz [18], CellTrp [34], ASNet [64], MMPSO-S [33] for TNBC[50], and UNet [55], SCAN [79], STAN [61], RRC-Net [13],  $EU^2Net$  [58], CE-Net [27], and DAUNet [54] for UDIAT[75]. For AD 128 and 256, we compare our proposed method with UNet [32], AttnUNet [32], and NuSegNet [69]. Our proposed loss improves the Dice score of the best-performing architecture for AD 128 (NuSegNet [69]) and AD 256 (AttnUNet [32]) by 1.74 and 3.55, respectively.

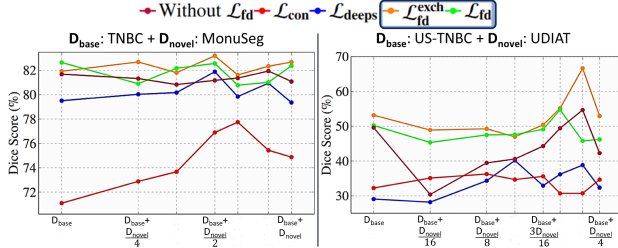


Figure 7. **Data Addition Dilemma.** An ablation showing the performance of various loss functions for histopathology and ultrasound datasets under the "Data Addition Dilemma" [62]. Data from  $D_{novel}$  is added to  $D_{base}$  to observe how losses handle distribution shifts.  $\mathcal{L}_{fd}^{exch}$  (orange) outperforms others in mitigating distribution shift when pooling data from multiple sources. The US-TNBC dataset has fewer samples, so we only added UDIAT dataset samples until their number matched (see Table 1.)

be derived from  $X$ .  $Z$  corresponds to the intermediate representations of the U-Net architecture [55], satisfying  $X \rightarrow Z$ . To ensure a strong correlation between  $Y$  and  $Z$ , the foreground features of  $Z$  must be highly discriminative from the background. In the U-Net architecture, the feature map  $F$  is represented by height, width, and channel. Ground-truth masks or clustering methods during training help identify indicators  $\tilde{y}$  that distinguish foreground from background features [63]. To enforce this discriminative property, we penalize the following loss.

**Definition 1. (Feature Discrepancy Loss):** Let  $F$  denote the features extracted from any network architecture and  $\tilde{y}$  represent the indicator variables identifying foreground features (the ground truth segmentation mask). We define the channel-averaged foreground features as  $F_g = \sum_k \left( \sum_{i,j} F[i, j, k] \otimes \tilde{y}[i, j, k] \right)$  and the channel-averaged background features as  $B_g = \sum_{i,j} F[i, j, k] \otimes (1 - \tilde{y}[i, j, k])$ , where  $\otimes$  denotes element-wise multiplication. The feature discrepancy loss is then given by:

$$\mathcal{L}_{fd} = -\log(\|F_g - B_g\|^2) \quad (1)$$

In the previous discussion,  $F_g - B_g$  represents the feature distance (FD) between foreground and background.

Penalizing this feature difference helps the model distinguish between foreground and background better, reducing over- and under-segmentation. In Lemma 1, we prove that the negative logarithm of the Dice score lower bounds the feature-distance loss, indicating that minimizing the feature-distance loss can improve Dice scores (Supplementary Sec B.1 for proof).

**Lemma 1.** Relationship between feature discrepancy loss  $\mathcal{L}_{fd}$ , segmentation Dice score, and constant  $k$  for feature vector  $F$  derived from image  $X$ :

$$-\log(\text{Dice} \times (k + 1)) \leq \mathcal{L}_{fd} \quad (2)$$

An increase in the Dice score results in a decrease of the lower bound, which allows for a decrease in  $\mathcal{L}_{fd}$ . As shown in Figure 1 (a), this relationship justifies the observed correlation between  $\mathcal{L}_{fd}$  and the Dice score for all models<sup>1</sup>.

**Axiom 2. (SGD Suboptimality for Convex Lipschitz Functions):** Let  $f : \mathbb{R}^d \rightarrow \mathbb{R}$  be a convex function with Lipschitz constant  $L$ . For step size  $\eta_t = \frac{1}{L\sqrt{T}}$  and  $T$  iterations, SGD achieves:  $\mathbb{E}[f(\theta_T) - f(\theta^*)] \leq \frac{CL}{\sqrt{T}}$ , where  $C > 0$  is a constant,  $\theta_T$  is the parameter at iteration  $T$ , and  $\theta^*$  is the optimal parameter.

Axiom 2 recalls a well-established fact that the suboptimality of Stochastic Gradient Descent (SGD) is bound by the Lipschitz constant ( $L$ ). Details of the proof of Axiom 2 can be found in [60] (page 187). In Lemma 2, we prove that minimizing  $\mathcal{L}_{fd}$  constrains the weight matrix  $W$  in each UNet layer by damping gradient updates (Supplementary Sec B.2 for proof). This prevents  $W$  from growing excessively to maximize feature discrepancy, which is crucial for medical imaging datasets that are significantly smaller than natural scene datasets. Large  $W$  risks data interpolation and memorization contribute to high variance, increasing the risk of overfitting. By enforcing feature separation without relying on a large  $\|W\|_2$ ,  $\mathcal{L}_{fd}$  acts as an implicit

<sup>1</sup> Although Lemma 1's bound may not be tight, experiments (Figure 2 (b) and Table 2) show a strict upper-lower bound relationship, indicating that minimizing  $\mathcal{L}_{fd}$  directly improves the Dice score.

regularizer, effectively bounding The Lipschitz constant  $L$  and improving generalization effect (see Axiom 2) empirically validated by higher test Dice scores (see Table 2). The trade-off between feature separation and weight norm is controlled by  $\gamma$ , implicitly determined by the optimization trajectory.  $\mathcal{L}_{fd}$  achieves an optimal balance, reducing overfitting while preserving discriminative power.

**Lemma 2. (Weight Norm Bound via Feature Discrepancy Loss):** *Let  $W \in \mathbb{R}^{d \times d}$  denote the weight matrix of a UNet layer producing features  $F = W \otimes x$ , where  $x \in \mathbb{R}^{d \times d}$  is the input to that layer. Then:*

$$\mathcal{L}_{fd} = -\log(\|W \otimes (x_g - x_b)\|_2^2) \quad (3)$$

where  $x_g$  and  $x_b$  are foreground and background features of  $x$ , respectively. Minimizing  $\mathcal{L}_{fd}$  implicitly enforces an upper bound on the spectral norm  $\|W\|_2$ , reducing the layer’s Lipschitz constant and improving generalization.

### 3.2.1. Implementation details

**Segmentation Loss  $\mathcal{L}_{seg}$ .** To penalize spatial prediction,  $\mathcal{L}_{seg}$  integrates Dice loss [65] and Binary Cross Entropy (BCE) loss [31], both essential for image segmentation. These losses evaluate model performance by comparing expected and actual masks.  $\mathcal{L}_{seg}$  is a linear combination of Dice and BCE loss, as given in [58] (Supplementary Sec A for more details).

**Layer-wise Feature Discrepancy Loss  $\mathcal{L}_{fd}$  and hyperparameter  $\alpha$  regulation.** The U-Net architecture employs an encoder-decoder structure with skip connections, enabling the extraction of multi-scale features at varying spatial resolutions. We introduce  $\mathcal{L}_{fd}$  at each feature layer to enhance segmentation accuracy. It is to be observed that the feature dimension for each layer of UNet is different. For applying  $\mathcal{L}_{fd}$  to each layer, we max pool  $\tilde{y}$  to match the feature dimension of that particular layer to extract  $F_g$  and  $B_g$ . This approach strengthens the model’s discriminative power by encouraging distinct feature learning across layers, as illustrated in Fig. 1(b). A trainable hyperparameter  $\alpha$  is introduced to control the importance of each layer in the feature discrepancy loss  $\mathcal{L}_{fd}$ , with unique  $\alpha$  values assigned per layer. This balances segmentation accuracy  $\mathcal{L}_{seg}$  and feature discrepancy at each level. Ablation (Section 4.3) reports the final  $\alpha$  values, showing each layer’s contribution to improved segmentation performance.

**Warm-Starting  $\alpha$ .** In the initial model updates,  $\alpha$  values are set to zero, optimizing exclusively for  $\mathcal{L}_{seg}$  without factoring in the penalty function  $\mathcal{L}_{fd}$ . This method enables  $\alpha$  to progressively rise from zero to infinity, consistent with the literature [6]. This approach enables a seamless shift from a constrained to an unconstrained problem, allowing for a thorough exploration of the solution space. Starting with a small penalty helps to mitigate potential ill-conditioning associated with large penalties at the outset. We start with  $\alpha$

Dataset	Data Type	All Samples	Worst Off	Threshold
TNBC [50]	Histopathology	50	10	75.0
MoNuSeg [37]	Histopathology	44	25	70.0
UDIAT [75]	Ultrasound	163	35	25.5
US-TNBC	Ultrasound	15	10	65.5
AD [32]	Histopathology	10k	500	40.0

Table 1. **Summary of datasets.** “All Samples” denote all the test samples of the dataset, whereas “Worst Off” are the test samples with lower Dice scores. Threshold is an approximate estimate of the range of Dice score below which the “Worst Off” samples lie. set to 0, permitting the algorithm to iterate multiple times before activating  $\alpha$  for training.

## 4. Experiments

We begin by detailing the experimental setup, including datasets, architectures, and a novel triple-negative breast cancer segmentation dataset. Sec 4.1 4.3 show how Feature Discrepancy Loss improves segmentation across datasets. In Sec 5, we demonstrate its effectiveness in preserving performance despite distributional shifts.

**Setup.** We conduct experiments using four datasets: the TNBC dataset [50] with histopathology images featuring dense glandular tissues and indistinct boundaries; the MoNuSeg dataset [37], which includes Hematoxylin and Eosin-stained histopathology images; and a novel US-TNBC dataset comprising 15 ultrasound images of TNBC tissues collected in 2022-23, with ground truth masks generated using Fiji (more details in Supplementary Sec G). The UDIAT dataset [75] includes breast ultrasound images characterized by irregular tumor morphology and indistinct boundaries. Additionally, we evaluate an Alzheimer’s histopathology dataset [32] for tau protein segmentation, with AD  $256 \times 256$  and AD  $128 \times 128$  versions, where the former contains a more complex background. Causal mediation and control of  $\mathcal{L}_{fd}$  are independent of the neural network architecture. We assess three prominent U-Net variants: AttentionUNet [32], which employs gated attention mechanisms for improved segmentation; NucleiSegNet [39], designed for overlapping boundaries and varying nuclei sizes; and CMUNet [66], which combines multi-scale attention gates and a ConvMixer module to capture both global and local features (details in Supplementary Sec H).

### 4.1. Quantitative Results on individual datasets

The effects of  $\mathcal{L}_{fd}$  are detailed in Table 2, which presents results for all samples, as well as for the Worst-off and Best-off samples based on Dice scores. Table 1 presents the numbers of the best-off and worst-off samples utilized in our experiments. The worst-off samples are the samples with the lower dice scores than other samples (see Fig. 1 (a)) as seen without the application of  $\mathcal{L}_{fd}$ . The best-off samples are the direct opposite of the worst-off samples, and their count is equal to that of the worst-off samples. The threshold in

Table 1 is an estimate of the approximate value of Dice scores below which the selected worst-off samples lie. In the case of CMUNet on the US-TNBC dataset, a slight decrease in the Dice score (-0.23) for Best-off samples is offset by improvements in Worst-off samples as  $\mathcal{L}_{fd}$  increases the overall average performance while emphasizing the worst-off samples. On the new US-TNBC dataset,  $\mathcal{L}_{fd}$  results in higher overall Dice scores. The improvements corroborate the theoretical findings in Lemma 1. (*Takeaway:* Penalizing  $\mathcal{L}_{fd}$  enhances segmentation performance across models and datasets.)

## 4.2. Qualitative Results on individual datasets

Qualitative results for the TNBC, MoNuSeg, AD, US-TNBC, and UDIAT datasets are presented in Figures 4. The red-highlighted areas in the predicted masks without  $\mathcal{L}_{fd}$  indicate segmentation errors, while the green-highlighted regions reflect corrections made by applying  $\mathcal{L}_{fd}$ . These experiments illustrate how  $\mathcal{L}_{fd}$  enhances segmentation through boundary refinement and reducing segmentation errors. The resulting masks display sharper, more accurate contours of key structures, preserving fine details and ensuring better anatomical representation. From Fig. 5, we can see that the introduction of  $\mathcal{L}_{fd}$  significantly reduces the unnecessary activations and streamlines the focus of the model to the region of interest, thus enhancing the segmentation performance. (*Takeaway:* Penalizing for  $\mathcal{L}_{fd}$  results in sharper boundaries, improved detail preservation, and increased consistency in generated segmentation masks.)

## 4.3. Ablation Studies on Feature Discrepancy Loss and Dataset Performance

**Impact of the  $\alpha$  Parameter on Feature Discrepancy Loss.** As discussed in Section 3.2.1,  $\alpha$  is a trainable parameter that initially starts at zero and regulates the penalty of feature discrepancy loss,  $\mathcal{L}_{fd}$ , for each layer of the neural network; the final values of  $\alpha$  indicate that the layer with the highest value had the most influence on improving the overall dice scores (see Figure 2 (a)). Furthermore, applying  $\mathcal{L}_{fd}$  across all layers yielded consistently better Dice scores (+1.3–1.8% across datasets) compared to selective layers (Enc 1, Dec 4, Bot), indicating that refined features from earlier layers enhance the discriminative quality of the final segmentation output.

**Comparison with State-of-the-Art Models.** For the TNBC [50], UDIAT [75], and MoNuSeg [37] datasets, our method achieves Dice score improvements of +0.96 (TNBC), +0.74 (MoNuSeg), and +0.75 (UDIAT) compared to CMUNet [66] and NucleiSegNet [39], demonstrating the effectiveness of penalizing feature discrepancy in modalities with high foreground-background similarity. For AD, larger patches ( $256 \times 256$  pixels) capture broader context, including background and neighboring pixels, while

smaller patches ( $128 \times 128$  pixels) focus primarily on plaque regions with limited context. Using the same experimental setup as [32], we observe performance improvements in AttnUNet [32] and NucleiSegNet [39] with the incorporation of  $\mathcal{L}_{fd}$ , as shown in Fig. 6.

**Changes in  $\mathcal{L}_{fd}$  and Dice scores at the sample level.** In Figure 2 (a), a trend between  $\mathcal{L}_{fd}$  and Dice is noted, with some samples exhibiting poor scores in both metrics. Figure 2 (b) presents a frequency plot for  $\mathcal{L}_{fd}$  (orange) and Dice (blue). A shift in  $\mathcal{L}_{fd}$  to lower values and Dice scores to higher values is observed, indicating a significant improvement in Dice scores at the sample level. This can also be seen in Supplementary Sec C that the samples move towards a lower  $\mathcal{L}_{fd}$  and a higher Dice score region in the  $\mathcal{L}_{fd}$  vs Dice plot. We also validate that the experiments are statistically significant in Supplementary Sec F.

**Performance comparison of various loss functions under noisy data.** Supplementary Sec I highlights the robustness of  $\mathcal{L}_{fd}$  over other loss functions due to the disentanglement between the foreground-background features, ensuring robust discriminative features under noisy data conditions.

## 5. Mitigating Data Distribution Shifts Under Assumed Exchangeability

Recent work emphasizes expanding medical imaging datasets by pooling data from multiple sources [17]. While early efforts apply invariant representation learning to handle covariate shifts, they often address only limited factors. The **Data Addition Dilemma** [62], underscores a critical issue: increasing training data size across sources can induce distributional shifts that degrade model performance. Traditional methods based on independent and identically distributed (i.i.d.) assumptions fail in cross-dataset scenarios. *Why i.i.d. is not realistic?* While the i.i.d. assumption is standard in most machine learning pipelines and often effective, it becomes overly restrictive in data addition scenarios. Exchangeability, being a weaker and more realistic assumption, better reflects the practical data generation process. For instance, in curating datasets like US-TNBC, new samples often depend on previously collected batches, violating i.i.d. but remaining consistent with exchangeability.

This challenge arises when combining a novel dataset,  $\mathcal{D}_{\text{novel}}$ , with a base dataset,  $\mathcal{D}_{\text{base}}$ , as their joint use violates i.i.d. assumptions. To address this, we leverage **exchangeability**, which extends beyond i.i.d. by ensuring that the joint distribution remains invariant under index permutations (Definition 2). By treating  $\mathcal{D}_{\text{base}}$  and  $\mathcal{D}_{\text{novel}}$  as exchangeable, we design a modified penalty loss function spanning both datasets. This ensures that discrepancies between foreground and background features across datasets remain comparable to within-dataset discrepancies, mitigating distributional shifts effectively. Algorithm 1 (Supplementary Sec D) outlines the training process using  $\mathcal{L}_{fd}^{\text{exh}}$ .

Model	Dataset	$\mathcal{L}_{fd}$	Worst Off Samples				Best Off Samples				All Samples			
			Dice	$\Delta$ Dice	IoU	$\Delta$ IoU	Dice	$\Delta$ Dice	IoU	$\Delta$ IoU	Dice	$\Delta$ Dice	IoU	$\Delta$ IoU
AttnUNet [32]	UDIAT	$\times$	22.42	+0.9	29.47	+0.8	75.86	+1.4	68.46	+1.0	67.21	+1.7	35.61	+2.8
		$\checkmark$	<b>23.28</b>		<b>30.31</b>		<b>77.29</b>		<b>69.50</b>		<b>68.96</b>		<b>38.43</b>	
	TNBC	$\times$	77.88		68.64		85.82		74.38		80.61		67.79	
		$\checkmark$	<b>77.86</b>	0.0	<b>68.66</b>	+0.0	<b>86.25</b>	+0.4	<b>77.57</b>	+3.2	<b>81.16</b>	+0.5	<b>69.19</b>	+1.4
CMUNet [66]	MoNuSeg	$\times$	66.03	+2.5	52.38	+0.7	82.57	+1.0	73.48	+1.0	75.92	+2.0	61.28	+1.6
		$\checkmark$	<b>68.61</b>		<b>53.06</b>		<b>83.62</b>		<b>74.50</b>		<b>77.97</b>		<b>62.87</b>	
	AD 256	$\times$	56.35	+1.3	31.92	+1.2	81.34	+4.3	70.88	+2.0	61.14	+3.5	43.87	+2.8
		$\checkmark$	<b>57.67</b>		<b>33.10</b>		<b>85.64</b>		<b>72.93</b>		<b>64.69</b>		<b>46.67</b>	
NuSegNet [39]	UDIAT	$\times$	31.56	+1.6	26.58	+1.6	90.88	+4.4	88.25	+1.8	81.85	+2.4	69.87	+3.1
		$\checkmark$	<b>33.19</b>		<b>28.17</b>		<b>95.32</b>		<b>90.01</b>		<b>84.22</b>		<b>73.02</b>	
	US-TNBC	$\times$	25.08	+1.9	21.44	+0.9	86.27	-0.2	68.09	+1.3	49.59	+0.6	34.53	+2.0
		$\checkmark$	<b>26.94</b>		<b>22.35</b>		<b>86.04</b>		<b>69.35</b>		<b>50.22</b>		<b>36.52</b>	
NuSegNet [39]	TNBC	$\times$	77.29	+2.1	68.00	+0.4	86.49	+0.3	71.29	+1.3	81.69	+1.0	69.22	+1.4
		$\checkmark$	<b>79.40</b>		<b>68.42</b>		<b>88.82</b>		<b>72.58</b>		<b>82.65</b>		<b>70.58</b>	
	MoNuSeg	$\times$	63.95	+0.7	50.05	+2.1	84.61	+0.3	70.40	+1.2	80.95	+0.7	67.91	+0.7
		$\checkmark$	<b>64.61</b>		<b>52.11</b>		<b>84.96</b>		<b>71.65</b>		<b>81.69</b>		<b>68.65</b>	
NuSegNet [39]	AD 256	$\times$	32.55	+3.2	23.19	+2.3	64.75	+6.4	46.28	+5.1	51.15	+5.4	36.17	+4.4
		$\checkmark$	<b>35.78</b>		<b>25.46</b>		<b>71.15</b>		<b>51.35</b>		<b>56.57</b>		<b>40.61</b>	

Table 2. **Ablation study on the application of  $\mathcal{L}_{fd}$ .** The improvement for low dice (Worst Off), high dice (Best Off), and all test samples (All Samples) is evident after applying  $\mathcal{L}_{fd}$ . NucleiSegNet [32] (histopathology) is not applicable to UDIAT and US-TNBC, while CMUNet [66] (ultrasound) does not apply to TNBC. Attention UNet [32] performs poorly on US-TNBC (Dice: 12.96). Changes in Dice ( $\Delta$  Dice) and IoU ( $\Delta$  IoU) are shown across all test settings.

**Definition 2. (Feature Discrepancy Loss under assumed exchangeability):**  $F_g(\mathcal{D})/B_g(\mathcal{D})$  represents foreground/background features from a randomly sampled dataset  $\mathcal{D}$ , which can be either  $\mathcal{D}_{novel}$  or  $\mathcal{D}_{base}$  dataset.

$$\mathcal{L}_{fd}^{exh} = -\log \left( \|F_g(\mathcal{D}_{base}) - B_g(\mathcal{D}_{novel})\|^2 + \|F_g(\mathcal{D}_{novel}) - B_g(\mathcal{D}_{base})\|^2 \right) \quad (4)$$

## 5.1. Experiments on Data Addition Dilemma

We selected TNBC as our base dataset, denoted as  $\mathcal{D}_{base}$ , using the MoNuSeg dataset as our novel dataset, labeled  $\mathcal{D}_{novel}$ . We added samples from MoNuSeg sequentially, to  $\mathcal{D}_{base}$  (For example, in the first setup we use  $\mathcal{D}_{base} + \frac{\mathcal{D}_{novel}}{16}$  while testing it on  $\mathcal{D}_{base}$ , in the next setup we use  $\mathcal{D}_{base} + \frac{\mathcal{D}_{novel}}{8}$  while testing it on  $\mathcal{D}_{base}$  and so on). All evaluations were performed on  $\mathcal{D}_{base}$ . Similarly, for the ultrasound datasets, we designated US-TNBC as  $\mathcal{D}_{base}$  and UDIAT as  $\mathcal{D}_{novel}$ , with samples from UDIAT added in batches of 15 images. We compared three methods: a naive method without penalties, a method penalizing for  $\mathcal{L}_{fd}$ , and a method penalizing for  $\mathcal{L}_{fd} + \mathcal{L}_{fd}^{exh}$ . We compare these three losses with the existing losses that deal with disentanglement ( $\mathcal{L}_{con}$ [11]) and layer-wise supervision ( $\mathcal{L}_{deeps}$ [19]). Notably, the naive method,  $\mathcal{L}_{con}$ [11] and  $\mathcal{L}_{deeps}$ [19] exhibited a decrease in test set accuracy on  $\mathcal{D}_{base}$  as more samples

from  $\mathcal{D}_{novel}$  were incorporated, consistent with the findings of [62].  $\mathcal{L}_{fd} + \mathcal{L}_{fd}^{exh}$  resulted in an overall performance improvement, as illustrated in Fig. 7. While  $\mathcal{L}_{fd}^{exh}$  shares conceptual similarity with local/pixel-wise contrastive losses [11], Fig. 7 shows contrastive loss ( $\mathcal{L}_{con}$ ) suffers significant performance drops (7–19%). This aligns with prior findings (e.g., Sec. 2 of [3]) showing contrastive losses require complex modifications to handle data addition and distribution shifts due to strong i.i.d. assumptions, making the weaker exchangeability assumption more realistic.

## 6. Conclusion

Data scarcity is a major challenge in medical imaging. To address this, our research introduces a novel feature discrepancy penalty function ( $\mathcal{L}_{fd}$ ) that enhances segmentation performance across modalities like histopathology and ultrasound. Our method outperforms existing models and baselines, showing improved Dice scores for both the worst-off and best-off samples. To tackle the lack of datasets for triple-negative breast cancer (TNBC), we introduced a new ultrasound dataset focused on TNBC.  $\mathcal{L}_{fd}$  reduces erroneous activation maps, enabling models to focus on relevant spatial regions more effectively. This is particularly impactful in the ‘‘Data Addition Dilemma’’ scenario, where pooling data from multiple sources introduces distribution shifts that degrade model performance. A modified version,  $\mathcal{L}_{fd}^{excg}$ , incorporates feature exchangeability to miti-

gate these shifts. Future work will explore distribution shift dynamics and extend the application of  $\mathcal{L}_{fd}$  to multiclass medical image generation tasks.

## References

- [1] Cancer en algérie: 65 000 nouveaux cas depuis début 2021, 2020. Accessed: 2020-12-01.
- [2] Mohsen Ahmadi, Masoumeh Farhadi Nia, Sara Asgarian, Kasra Danesh, Elyas Irankhah, Ahmad Gholizadeh Lonbar, and Abbas Sharifi. Comparative analysis of segment anything model and u-net for breast tumor detection in ultrasound and mammography images. *arXiv preprint arXiv:2306.12510*, 2023.
- [3] Aditya Kumar Akash, Vishnu Suresh Lokhande, Sathya N Ravi, and Vikas Singh. Learning invariant representations using inverse contrastive loss. In *Proceedings of the AAAI Conference on Artificial Intelligence*, pages 6582–6591, 2021.
- [4] Elias Bareinboim and Judea Pearl. Causal inference and the data-fusion problem. *Proceedings of the National Academy of Sciences*, 113(27):7345–7352, 2016.
- [5] Scott Barnett, Zac Brannelly, Stefanus Kurniawan, and Sheng Wong. Fine-tuning or fine-failing? debunking performance myths in large language models. *arXiv preprint arXiv:2406.11201*, 2024.
- [6] Dimitri P Bertsekas. Nonlinear programming. *Journal of the Operational Research Society*, 48(3):334–334, 1997.
- [7] Serge Beucher and Fernand Meyer. The morphological approach to segmentation: the watershed transformation. In *Mathematical morphology in image processing*, pages 433–481. CRC Press, 2018.
- [8] Hu Cao, Yueyue Wang, Joy Chen, Dongsheng Jiang, Xiaopeng Zhang, Qi Tian, and Manning Wang. Swin-unet: Unet-like pure transformer for medical image segmentation. In *European conference on computer vision*, pages 205–218. Springer, 2022.
- [9] Yair Carmon, Aditi Raghunathan, Ludwig Schmidt, John C Duchi, and Percy S Liang. Unlabeled data improves adversarial robustness. *Advances in neural information processing systems*, 32, 2019.
- [10] Daniel C Castro, Ian Walker, and Ben Glocker. Causality matters in medical imaging. *Nature Communications*, 11(1): 3673, 2020.
- [11] Krishna Chaitanya, Ertunc Erdil, Neerav Karani, and Ender Konukoglu. Contrastive learning of global and local features for medical image segmentation with limited annotations. *Advances in neural information processing systems*, 33:12546–12558, 2020.
- [12] O Chapelle, B Schölkopf, and A Zien. *Semi-supervised learning* mit press cambridge, 2006.
- [13] Gongping Chen, Yu Dai, and Jianxun Zhang. Rrcnet: Refinement residual convolutional network for breast ultrasound images segmentation. *Engineering Applications of Artificial Intelligence*, 117:105601, 2023.
- [14] Jieneng Chen, Yongyi Lu, Qihang Yu, Xiangde Luo, Ehsan Adeli, Yan Wang, Le Lu, Alan L Yuille, and Yuyin Zhou. Transunet: Transformers make strong encoders for medical image segmentation. *arXiv preprint arXiv:2102.04306*, 2021.
- [15] Liang-Chieh Chen, George Papandreou, Iasonas Kokkinos, Kevin Murphy, and Alan L Yuille. Semantic image segmentation with deep convolutional nets and fully connected crfs. *arXiv preprint arXiv:1412.7062*, 2014.
- [16] Richard J Chen, Ming Y Lu, Wei-Hung Weng, Tiffany Y Chen, Drew FK Williamson, Trevor Manz, Maha Shady, and Faisal Mahmood. Multimodal co-attention transformer for survival prediction in gigapixel whole slide images. In *Proceedings of the IEEE/CVF International Conference on Computer Vision*, pages 4015–4025, 2021.
- [17] Sotirios Panagiotis Chytas, Vishnu Suresh Lokhande, and Vikas Singh. Pooling image datasets with multiple covariate shift and imbalance. In *The Twelfth International Conference on Learning Representations*, 2024.
- [18] Nirmal Das, Satadal Saha, Mita Nasipuri, Subhadip Basu, and Tapabrata Chakraborti. Deep-fuzz: A synergistic integration of deep learning and fuzzy water flows for fine-grained nuclei segmentation in digital pathology. *Plos one*, 18(6):e0286862, 2023.
- [19] Qi Dou, Hao Chen, Yueming Jin, Lequan Yu, Jing Qin, and Pheng-Ann Heng. 3d deeply supervised network for automatic liver segmentation from ct volumes. In *Medical Image Computing and Computer-Assisted Intervention—MICCAI 2016: 19th International Conference, Athens, Greece, October 17–21, 2016, Proceedings, Part II 19*, pages 149–157. Springer, 2016.
- [20] Chaitanya Dwivedi, Shima Nofallah, Maryam Pouryahya, Janani Iyer, Kenneth Leidal, Chuhan Chung, Timothy Watkins, Andrew Billin, Robert Myers, John Abel, et al. Multi stain graph fusion for multimodal integration in pathology. In *Proceedings of the IEEE/CVF Conference on Computer Vision and Pattern Recognition*, pages 1835–1845, 2022.
- [21] Ewan Evain, Caroline Raynaud, Cybèle Ciofolo-Veit, Alexandre Popoff, Thomas Caramella, Pascal Kbaier, Corinne Balleyguier, Sana Harguem-Zayani, Héloïse Dapvril, Luc Ceugnart, et al. Breast nodule classification with two-dimensional ultrasound using mask-rcnn ensemble aggregation. *Diagnostic and Interventional Imaging*, 102(11):653–658, 2021.
- [22] Zunlei Feng, Zhonghua Wang, Xinchao Wang, Yining Mao, Thomas Li, Jie Lei, Yuexuan Wang, and Mingli Song. Mutual-complementing framework for nuclei detection and segmentation in pathology image. In *Proceedings of the IEEE/CVF International Conference on Computer Vision (ICCV)*, pages 4036–4045, 2021.
- [23] Francois Fleuret et al. Uncertainty reduction for model adaptation in semantic segmentation. In *Proceedings of the IEEE/CVF Conference on Computer Vision and Pattern Recognition*, pages 9613–9623, 2021.
- [24] Yinghua Fu, Junfeng Liu, and Jun Shi. Tsca-net: Transformer based spatial-channel attention segmentation network for medical images. *Computers in Biology and Medicine*, 170:107938, 2024.



- [25] Evgin Goceri. Medical image data augmentation: techniques, comparisons and interpretations. *Artificial Intelligence Review*, 56(11):12561–12605, 2023.
- [26] Shizhan Gong, Yuan Zhong, Yuqi Gong, Nga Yan Chan, Wenao Ma, Calvin Hoi-Kwan Mak, Jill Abrigo, and Qi Dou. Segmentation of tiny intracranial hemorrhage via learning-to-rank local feature enhancement. In *2024 IEEE International Symposium on Biomedical Imaging (ISBI)*, pages 1–5. IEEE, 2024.
- [27] Zaiwang Gu, Jun Cheng, Huazhu Fu, Kang Zhou, Huaying Hao, Yitian Zhao, Tianyang Zhang, Shenghua Gao, and Jiang Liu. Ce-net: Context encoder network for 2d medical image segmentation. *IEEE transactions on medical imaging*, 38(10):2281–2292, 2019.
- [28] Sheng He, Rina Bao, Jingpeng Li, Jeffrey Stout, Atle Bjornerud, P Ellen Grant, and Yangming Ou. Computer-vision benchmark segment-anything model (sam) in medical images: Accuracy in 12 datasets. *arXiv preprint arXiv:2304.09324*, 2023.
- [29] Xingjian He, Jing Liu, Jun Fu, Xinxin Zhu, Jinqiao Wang, and Hanqing Lu. Consistent-separable feature representation for semantic segmentation. In *Proceedings of the AAAI Conference on Artificial Intelligence*, pages 1531–1539, 2021.
- [30] Rashadul Islam Sumon, Subrata Bhattacharjee, Yeong-Byn Hwang, Hafizur Rahman, Hee-Cheol Kim, Wi-Sun Ryu, Dong Min Kim, Nam-Hoon Cho, and Heung-Kook Choi. Densely convolutional spatial attention network for nuclei segmentation of histological images for computational pathology. *Frontiers in Oncology*, 13:1009681, 2023.
- [31] Shruti Jadon. A survey of loss functions for semantic segmentation. In *2020 IEEE conference on computational intelligence in bioinformatics and computational biology (CIBCB)*, pages 1–7. IEEE, 2020.
- [32] Gabriel Jiménez, Anuradha Kar, Mehdi Ounissi, Léa Ingrassia, Susana Boluda, Benoît Delatour, Lev Stimmer, and Daniel Racoceanu. Visual deep learning-based explanation for neuritic plaques segmentation in alzheimer’s disease using weakly annotated whole slide histopathological images. In *International Conference on Medical Image Computing and Computer-Assisted Intervention*, pages 336–344. Springer, 2022.
- [33] Anusree Kanadath, J Angel Arul Jothi, and Siddhaling Urolagin. Multilevel multiobjective particle swarm optimization guided superpixel algorithm for histopathology image detection and segmentation. *Journal of Imaging*, 9(4):78, 2023.
- [34] Matthew R Keaton, Ram J Zaveri, and Gianfranco Doretto. Celltranspose: Few-shot domain adaptation for cellular instance segmentation. In *Proceedings of the IEEE/CVF Winter Conference on Applications of Computer Vision*, pages 455–466, 2023.
- [35] Alexander Kirillov, Eric Mintun, Nikhila Ravi, Hanzi Mao, Chloe Rolland, Laura Gustafson, Tete Xiao, Spencer Whitehead, Alexander C Berg, Wan-Yen Lo, et al. Segment anything. In *Proceedings of the IEEE/CVF International Conference on Computer Vision*, pages 4015–4026, 2023.
- [36] Ananya Kumar, Aditi Raghunathan, Robbie Jones, Tengyu Ma, and Percy Liang. Fine-tuning can distort pretrained features and underperform out-of-distribution. *arXiv preprint arXiv:2202.10054*, 2022.
- [37] Neeraj Kumar, Ruchika Verma, Deepak Anand, Yanning Zhou, Omer Fahri Onder, Efstratios Tsougenis, Hao Chen, Pheng-Ann Heng, Jiahui Li, Zhiqiang Hu, et al. A multi-organ nucleus segmentation challenge. *IEEE transactions on medical imaging*, 39(5):1380–1391, 2019.
- [38] Andrew Lagree, Majidreza Mohebpour, Nicholas Meti, Khadijeh Saednia, Fang-I Lu, Elzbieta Slodkowska, Sonal Gandhi, Eileen Rakovitch, Alex Shenfield, Ali Sadeghi-Naini, et al. A review and comparison of breast tumor cell nuclei segmentation performances using deep convolutional neural networks. *Scientific Reports*, 11(1):8025, 2021.
- [39] Shyam Lal, Devikalyan Das, Kumar Alabhya, Anirudh Kanfade, Aman Kumar, and Jyoti Kini. Nucleisegnet: Robust deep learning architecture for the nuclei segmentation of liver cancer histopathology images. *Computers in Biology and Medicine*, 128:104075, 2021.
- [40] Zhengqin Li and Jiansheng Chen. Superpixel segmentation using linear spectral clustering. In *Proceedings of the IEEE conference on computer vision and pattern recognition*, pages 1356–1363, 2015.
- [41] Runqi Lin, Chaojian Yu, Bo Han, and Tongliang Liu. On the over-memorization during natural, robust and catastrophic overfitting. *arXiv preprint arXiv:2310.08847*, 2023.
- [42] Vishnu Suresh Lokhande, Rudrasis Chakraborty, Sathya N Ravi, and Vikas Singh. Equivariance allows handling multiple nuisance variables when analyzing pooled neuroimaging datasets. In *Proceedings of the IEEE/CVF Conference on Computer Vision and Pattern Recognition*, pages 10432–10441, 2022.
- [43] Jonathan Long, Evan Shelhamer, and Trevor Darrell. Fully convolutional networks for semantic segmentation. In *Proceedings of the IEEE conference on computer vision and pattern recognition*, pages 3431–3440, 2015.
- [44] Alan Lundgard. Measuring justice in machine learning. *arXiv preprint arXiv:2009.10050*, 2020.
- [45] Priyanka Malhotra, Sheifali Gupta, Deepika Koundal, Atef Zaguia, and Wegayehu Enbeyle. [retracted] deep neural networks for medical image segmentation. *Journal of Healthcare Engineering*, 2022(1):9580991, 2022.
- [46] Maciej A Mazurowski, Haoyu Dong, Hanxue Gu, Jichen Yang, Nicholas Konz, and Yixin Zhang. Segment anything model for medical image analysis: an experimental study. *Medical Image Analysis*, 89:102918, 2023.
- [47] Daniel Moyer, Shuyang Gao, Rob Brekelmans, Aram Galstyan, and Greg Ver Steeg. Invariant representations without adversarial training. *Advances in neural information processing systems*, 31, 2018.
- [48] Daniel Moyer, Greg Ver Steeg, Chantal MW Tax, and Paul M Thompson. Scanner invariant representations for diffusion mri harmonization. *Magnetic resonance in medicine*, 84(4): 2174–2189, 2020.
- [49] Preetum Nakkiran, Gal Kaplun, Yamini Bansal, Tristan Yang, Boaz Barak, and Ilya Sutskever. Deep double descent: Where bigger models and more data hurt. *Journal of Statistical Mechanics: Theory and Experiment*, 2021(12):124003, 2021.

- [50] Peter Naylor, Marick Laé, Fabien Rey, and Thomas Walter. Segmentation of nuclei in histopathology images by deep regression of the distance map. *IEEE transactions on medical imaging*, 38(2):448–459, 2018.
- [51] Avital Oliver, Augustus Odena, Colin A Raffel, Ekin Dogus Cubuk, and Ian Goodfellow. Realistic evaluation of deep semi-supervised learning algorithms. *Advances in neural information processing systems*, 31, 2018.
- [52] Judea Pearl. *Causality*. Cambridge university press, 2009.
- [53] Alethea Power, Yuri Burda, Harri Edwards, Igor Babuschkin, and Vedant Misra. Grokking: Generalization beyond overfitting on small algorithmic datasets. *arXiv preprint arXiv:2201.02177*, 2022.
- [54] Payel Pramanik, Ayush Roy, Erik Cuevas, Marco Perez-Cisneros, and Ram Sarkar. Dau-net: Dual attention-aided u-net for segmenting tumor in breast ultrasound images. *Plos one*, 19(5):e0303670, 2024.
- [55] Olaf Ronneberger, Philipp Fischer, and Thomas Brox. U-net: Convolutional networks for biomedical image segmentation. In *Medical Image Computing and Computer-Assisted Intervention—MICCAI 2015: 18th International Conference, Munich, Germany, October 5–9, 2015, Proceedings, Part III 18*, pages 234–241. Springer, 2015.
- [56] Ayush Roy, Payel Pramanik, Sohom Ghosal, Daria Valenkova, Dmitrii Kaplun, and Ram Sarkar. Gru-net: Gaussian attention aided dense skip connection based multi-resnet for breast histopathology image segmentation. In *Annual Conference on Medical Image Understanding and Analysis*, pages 300–313. Springer, 2024.
- [57] Ayush Roy, Payel Pramanik, Dmitrii Kaplun, Sergei Antonov, and Ram Sarkar. Awgunet: Attention-aided wavelet guided u-net for nuclei segmentation in histopathology images. In *2024 IEEE International Symposium on Biomedical Imaging (ISBI)*, pages 1–4, 2024.
- [58] Ayush Roy, Payel Pramanik, and Ram Sarkar. Eu 2-net: A parameter efficient ensemble model with attention-aided triple feature fusion for tumor segmentation in breast ultrasound images. *IEEE Transactions on Instrumentation and Measurement*, 2024.
- [59] Bernhard Schölkopf, Dominik Janzing, Jonas Peters, Eleni Sgouritsa, Kun Zhang, and Joris Mooij. On causal and anti-causal learning. *arXiv preprint arXiv:1206.6471*, 2012.
- [60] Shai Shalev-Shwartz and Shai Ben-David. *Understanding Machine Learning: From Theory to Algorithms*. Cambridge University Press, 2014.
- [61] Bryar Shareef, Min Xian, and Aleksandar Vakanski. Stan: Small tumor-aware network for breast ultrasound image segmentation. In *2020 IEEE 17th international symposium on biomedical imaging (ISBI)*, pages 1–5. IEEE, 2020.
- [62] Judy Hanwen Shen, Inioluwa Deborah Raji, and Irene Y Chen. The data addition dilemma. *arXiv preprint arXiv:2408.04154*, 2024.
- [63] Zachary Sims, Luke Strgar, Dharani Thirumalaisamy, Robert Heussner, Guillaume Thibault, and Young Hwan Chang. Seg: Segmentation evaluation in absence of ground truth labels. *bioRxiv*, 2023.
- [64] Anu Singha and Mrinal Kanti Bhowmik. Alexsegnet: an accurate nuclei segmentation deep learning model in microscopic images for diagnosis of cancer. *Multimedia Tools and Applications*, 82(13):20431–20452, 2023.
- [65] Toufique A Soomro, Ahmed J Afifi, Junbin Gao, Olaf Hellwich, Manoranjan Paul, and Lihong Zheng. Strided u-net model: Retinal vessels segmentation using dice loss. In *2018 Digital Image Computing: Techniques and Applications (DICTA)*, pages 1–8. IEEE, 2018.
- [66] Fenghe Tang, Lingtao Wang, Chunping Ning, Min Xian, and Jianrui Ding. Cmu-net: A strong convmixer-based medical ultrasound image segmentation network. In *2023 IEEE 20th International Symposium on Biomedical Imaging (ISBI)*, pages 1–5, 2023.
- [67] Paul M Thompson, Jason L Stein, Sarah E Medland, Derek P Hibar, Alejandro Arias Vasquez, Miguel E Renteria, Roberto Toro, Neda Jahanshad, Gunter Schumann, Barbara Franke, et al. The ENIGMA Consortium: large-scale collaborative analyses of neuroimaging and genetic data. *Brain imaging and behavior*, 8:153–182, 2014.
- [68] Nikhil Kumar Tomar, Debesh Jha, Ulas Bagci, and Sharib Ali. Tganet: Text-guided attention for improved polyp segmentation. In *International Conference on Medical Image Computing and Computer-Assisted Intervention*, pages 151–160. Springer, 2022.
- [69] Nikhil Kumar Tomar, Annie Shergill, Brandon Rieders, Ulas Bagci, and Debesh Jha. Transresu-net: Transformer based resu-net for real-time colonoscopy polyp segmentation. *arXiv preprint arXiv:2206.08985*, 2022.
- [70] Rachida Touami and Nacéra Benamrane. Microcalcification detection in mammograms using particle swarm optimization and probabilistic neural network. *Computación y Sistemas*, 25(2):369–379, 2021.
- [71] Jeya Maria Jose Valanarasu, Poojan Oza, Ilker Hacihaliloglu, and Vishal M Patel. Medical transformer: Gated axial-attention for medical image segmentation. In *Medical Image Computing and Computer Assisted Intervention—MICCAI 2021: 24th International Conference, Strasbourg, France, September 27–October 1, 2021, Proceedings, Part I 24*, pages 36–46. Springer, 2021.
- [72] Saad Wazir and Muhammad Moazam Fraz. Histoseg: Quick attention with multi-loss function for multi-structure segmentation in digital histology images. In *2022 12th International Conference on Pattern Recognition Systems (ICPRS)*, pages 1–7. IEEE, 2022.
- [73] Hanqing Xu, Ming Yang, Liuyuan Deng, Yeqiang Qian, and Chunxiang Wang. Neutral cross-entropy loss based unsupervised domain adaptation for semantic segmentation. *IEEE Transactions on Image Processing*, 30:4516–4525, 2021.
- [74] Qing Xu, Wenwei Kuang, Zeyu Zhang, Xueyao Bao, Haoran Chen, and Wenting Duan. Sppnet: A single-point prompt network for nuclei image segmentation. *arXiv preprint arXiv:2308.12231*, 2023.
- [75] Moi Hoon Yap, Gerard Pons, Joan Martí, Sergi Ganau, Melcior Sentis, Reyer Zwiggelaar, Adrian K Davison, and Robert Martí. Automated breast ultrasound lesions detection using convolutional neural networks. *IEEE journal of biomedical and health informatics*, 22(4):1218–1226, 2017.

- [76] Srikar Yellapragada, Alexandros Graikos, Prateek Prasanna, Tahsin Kurc, Joel Saltz, and Dimitris Samaras. Pathldm: Text conditioned latent diffusion model for histopathology. In *Proceedings of the IEEE/CVF Winter Conference on Applications of Computer Vision*, pages 5182–5191, 2024.
- [77] Xue Ying. An overview of overfitting and its solutions. In *Journal of physics: Conference series*, page 022022. IOP Publishing, 2019.
- [78] Rammah Yousef, Shakir Khan, Gaurav Gupta, Tamanna Siddiqui, Bader M Albahlal, Saad Abdullah Alajlan, and Mohd Anul Haq. U-net-based models towards optimal mr brain image segmentation. *Diagnostics*, 13(9):1624, 2023.
- [79] Bofei Zhang, Le Lu, Jianhua Yao, Xiaoguang Wang, and Ronald M Summers. Attention-based cnn for kl grade classification: Data from the osteoarthritis initiative. In *2020 IEEE 17th International Symposium on Biomedical Imaging (ISBI)*, pages 1006–1009. IEEE, 2020.
- [80] Yanan Zhang, Jiangmeng Li, Lixiang Liu, and Wenwen Qiang. Rethinking misalignment in vision-language model adaptation from a causal perspective. *arXiv preprint arXiv:2410.12816*, 2024.
- [81] Tianze Zhao, Zhijun Fan, Xintian Wang, Jinglong Tian, Menghan Yang, and Qiumei Pu. Comparison of cell image segmentation results based on unet and transformer. In *Third International Conference on Image Processing, Object Detection, and Tracking (IPODT 2024)*, pages 92–101. SPIE, 2024.
- [82] Yiyang Zhao, Jinjiang Li, Lu Ren, and Zheng Chen. Dtan: Diffusion-based text attention network for medical image segmentation. *Computers in Biology and Medicine*, 168: 107728, 2024.

# Is Exchangeability better than I.I.D to handle Data Distribution Shifts while Pooling Data for Data-scarce Medical image segmentation?

## Supplementary Material

### A. The segmentation loss

The Dice loss [65] and Binary Cross Entropy (BCE) loss [31] are crucial for image segmentation tasks, evaluating model performance by comparing predicted and actual masks. The dice loss ( $L_{dice}$ ) and the BCE loss ( $L_{bce}$ ) are defined in Eq. 5 and 6 respectively where  $y_{ijk}$  represents the ground truth label for pixel  $(i, j, k)$ ,  $\tilde{y}_{ijk}$  represents the predicted probability for pixel  $(i, j, k)$ ,  $\epsilon$  is a small constant added for numerical stability to avoid division by zero or taking the log of zero, and  $N$  is the total number of elements pixels.

$$L_{dice} = 1 - \frac{2 \sum_{i,j,k} y_{ijk} \cdot \tilde{y}_{ijk} + \epsilon}{\sum_{i,j,k} y_{ijk} + \sum_{i,j,k} \tilde{y}_{ijk} + \epsilon} \quad (5)$$

$$L_{bce} = -\frac{1}{N} \sum_{i,j,k} \left( y_{ijk} \cdot \log(\tilde{y}_{ijk}) + (1 - y_{ijk}) \cdot \log(1 - \tilde{y}_{ijk}) + \epsilon \right) \quad (6)$$

We use a linear combination of  $L_{dice}$  and  $L_{bce}$  as  $L_{seg}$  [58]. This can be seen in Eq. 7

$$L_{seg} = L_{dice} + L_{bce} \quad (7)$$

### B. Proofs

#### B.1. Lemma 1

**Lemma 3.** *Relationship between feature discrepancy loss  $\mathcal{L}_{fd}$ , segmentation Dice score, and constant  $k$  for feature vector  $F$  derived from image  $X$ :*

$$-\log(\text{Dice} \times (k+1)) \leq \mathcal{L}_{fd} \quad (8)$$

*Proof.* Let  $\otimes$  denote element-wise multiplication. Then we get the relation between Dice score, the predicted segmentation mask  $y$ , and the ground truth segmentation mask  $\tilde{y}$  as:

$$\sum_{i,j,k} \tilde{y}_{ijk} = \frac{\text{Dice}}{2} \times \frac{\sum_{i,j,k} y_{ijk} + \sum_{i,j,k} \tilde{y}_{ijk}}{\sum_{i,j,k} y_{ijk}} \quad (9)$$

(since  $\text{Dice} = \frac{2 \sum_{i,j,k} y_{ijk} \cdot \tilde{y}_{ijk} + \epsilon}{\sum_{i,j,k} y_{ijk} + \sum_{i,j,k} \tilde{y}_{ijk} + \epsilon}$ )

Now, simplifying FD (feature discrepancy) using Definition 1, we get:

$$FD = \frac{\|\sum_k (\sum_{i,j} F_{i,j,k} \otimes \tilde{y}_{i,j,k} - \sum_{i,j} F_{i,j,k} \otimes (1 - \tilde{y}_{i,j,k}))\|_2}{\|\sum_{i,j,k} F_{ijk}\|_2} \quad (10)$$

$$FD \leq \frac{\|2 \sum_{i,j,k} F_{i,j,k} \otimes \tilde{y}_{i,j,k}\|_2}{\|\sum_{i,j,k} F_{ijk}\|_2} + \frac{\|\sum_{i,j,k} F_{i,j,k}\|_2}{\|\sum_{i,j,k} F_{ijk}\|_2} \quad (11)$$

(using the triangle inequality).

Now, using Eq. 9 we get:

$$FD - 1 \leq \frac{\|\sum_{i,j,k} F_{i,j,k} \otimes \text{Dice} \times \frac{\sum_{i,j,k} y_{ijk} + \sum_{i,j,k} \tilde{y}_{ijk}}{\sum_{i,j,k} y_{ijk}}\|_2}{\|\sum_{i,j,k} F_{ijk}\|_2} \quad (12)$$

Since  $\sum_{i,j,k} \tilde{y}_{ijk}$  and  $\sum_{i,j,k} y_{ijk}$  are constants during testing, let  $\frac{\sum_{i,j,k} \tilde{y}_{ijk}}{\sum_{i,j,k} y_{ijk}} = k'$ :

$$-\log(FD) \geq -\log(\text{Dice} \times (k+1)) \quad (13)$$

(Taking  $-\log$  on both sides).

$$\mathcal{L}_{fd} \geq -\log(\text{Dice} \times (k+1)) \quad (14)$$

This completes the proof.  $\square$

#### B.2. Lemma 2

**Lemma 4. (Weight Norm Bound via Feature Discrepancy Loss):** *Let  $W \in \mathbb{R}^{d \times d}$  denote the weight matrix of a UNet layer producing features  $F = W \otimes x$ , where  $x \in \mathbb{R}^{d \times d}$  is the input to that layer. The relationship between  $\mathcal{L}_{fd}$  and  $W$  is given by:*

$$\mathcal{L}_{fd} = -\log(\|W \otimes (x_g - x_b)\|_2^2) \quad (15)$$

where  $x_g$  and  $x_b$  are foreground and background features of  $x$ , respectively. Minimizing  $\mathcal{L}_{fd}$  implicitly enforces an upper bound on the spectral norm  $\|W\|_2$ , reducing the layer's Lipschitz constant and improving generalization.

*Proof.* Let  $\Delta x = x_g - x_b$  denote the inherent foreground-background separation in the input space. The loss  $\mathcal{L}_{fd}$  incentivizes maximizing  $\|W \otimes \Delta x\|_2^2$  where  $\otimes$  is the hadamard product. Now we can frame the hadamard product in a different way to represent  $W \otimes \Delta x$  as  $W_{exp} \times \Delta x_{exp}$  where  $\times$  is matrix multiplication,  $W_{exp} \in \mathbb{R}^{d^2 \times d^2}$  is a diagonalized form of  $W$  and  $x_{exp} \in \mathbb{R}^{d^2 \times 1}$  is a reshaped form of  $x$ . The Lipschitz constant  $L$  of the layer  $F = W_{exp} \times x$  is the spectral norm of  $W_{exp}$ :

$$L = \|W_{exp}\|_2 = \sup_{\|x_{exp}\|_2=1} \|W_{exp} \times x_{exp}\|_2 \quad (16)$$

This measures the maximum amplification of the input by  $W_{exp}$ . To minimize  $\mathcal{L}_{fd}$ , the optimization ensures  $\|W_{exp} \times \Delta x_{exp}\|_2^2 \geq \gamma$  for some  $\gamma > 0$ . By Cauchy-Schwarz:

$$\|W_{exp} \times \Delta x_{exp}\|_2 \leq \|W_{exp}\|_2 \|\Delta x_{exp}\|_2. \quad (17)$$

Squaring both sides:

$$\gamma \leq \|W_{exp} \times \Delta x_{exp}\|_2^2 \leq \|W_{exp}\|_2^2 \|\Delta x_{exp}\|_2^2 \quad (18)$$

$$\implies \|W_{exp}\|_2 \geq \frac{\sqrt{\gamma}}{\|\Delta x_{exp}\|_2}. \quad (19)$$

Thus,  $\gamma$  defines the *minimum required separation* between foreground and background features.

The gradient of  $\mathcal{L}_{fd}$  with respect to  $W$  is:

$$\nabla_W \mathcal{L}_{fd} = -\frac{2}{\|W \otimes \Delta x\|_2^2} (W \otimes \Delta x)(\Delta x)^T. \quad (20)$$

The term  $\frac{1}{\|W \otimes \Delta x\|_2^2}$  acts as an *adaptive damping factor*: as  $\|W \otimes \Delta x\|_2^2$  increases (better separation), the gradient magnitude decreases. This prevents  $W$  from growing excessively to inflate separation artificially, thereby bounding  $\|W\|_2$  and thus  $\|W_{exp}\|_2$  (since  $W_{exp}$  is a diagonalized form of  $W$ ).

The network achieves  $\|W_{exp} \times \Delta x_{exp}\|_2^2 \geq \gamma$  with the smallest possible  $\|W\|_2$  (due to gradient damping) ensuring *lower variance model* (reduced sensitivity to input perturbations) and preventing overfitting. Furthermore, the Lipschitz constant  $L$ , is also reduced, indicating a *tighter generalization bounds* (the suboptimal error bound,  $\mathcal{E}_{gen} \propto L$  as seen in Axiom 2).  $\square$

### C. Qualitative analysis of Dice vs Feature discrepancy loss

Figure 8 shows the improvement in the Dice scores of the samples with a decrease in  $\mathcal{L}_{fd}$ . As we can see in the Dice

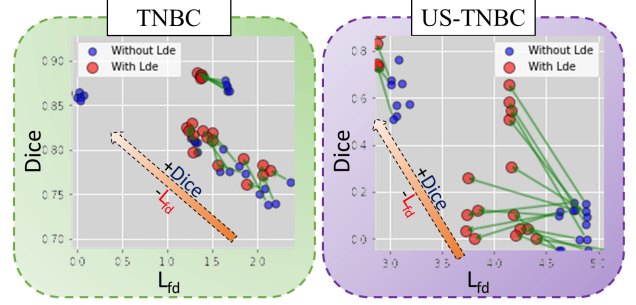


Figure 8. **The change in Dice scores with change in  $\mathcal{L}_{fd}$ .** The plot with axis as Dice score and  $\mathcal{L}_{fd}$  for samples of TNBC [50] and US-TNBC for the Bottleneck (Bot) layer of NucleiSegNet [39] and CMUNet [66] are plotted respectively. The green arrows indicate the movement of each point after the use of  $\mathcal{L}_{fd}$ . The red arrow indicates the overall movement of the majority of the samples.

vs  $\mathcal{L}_{fd}$  plot, as Dice score improves,  $\mathcal{L}_{fd}$  decreases, and the points move to the top left corner of the plot. The green arrows signify the movement of each sample (each test image) after the use of  $\mathcal{L}_{fd}$ . The red arrow indicates an overall movement of the samples highlighting the flow towards the top left corner (increase in Dice and decrease in  $\mathcal{L}_{fd}$ ). This signifies the importance of foreground and background feature disentanglement to ensure robust medical image segmentation under a data-scarce setting with complex backgrounds.

### D. Algorithmic explanation of exchangeable Feature discrepancy loss

The algorithmic explanation of  $\mathcal{L}_{fd}^{exh}$  for each iteration of training can be seen in Algorithm 1. Specifically, the foreground feature of image  $i$  ( $F_{g,i}$ ) pushes the background feature of image  $j$  ( $B_{g,j}$ ) in  $\mathcal{L}_{fd}^{exh}$ , while  $F_{g,j}$  simultaneously pushes  $B_{g,i}$  in  $\mathcal{L}_{fd}$ . This draws  $F_{g,i}$  and  $F_{g,j}$  closer, minimizing the distributional shift caused by differences in batch data sources.

---

#### Algorithm 1 $\mathcal{L}_{fd}^{exh}$ explained in Section 5

---

- 1: **Input:** Foreground features  $F_g$  and background features  $B_g$  for each image  $i$  in a batch of size  $n$
  - 2: **for** each training iteration **do**
  - 3:   **for**  $i \leftarrow 1$  to  $n$  **do**
  - 4:      $\mathcal{L}_{fd} = -\log(\|F_{g,i} - B_{g,i}\|_2)$    ▷ Penalizing feature distance of foreground and background for the same image
  - 5:      $\mathcal{L}_{fd}^{exh} = -\log(\|F_{g,i} - B_{g,i+k}\|_2)$    ▷ Where  $k$  is arbitrary and introduced after shuffling  $F_g$  and  $B_g$  to ensure  $F_{g,i}$  and  $F_{g,j}$  are closer by repelling  $B_{g,j}$
  - 6:      $L_i = \mathcal{L}_{fd} + \mathcal{L}_{fd}^{exh}$
  - 7:   **end for**
  - 8:   loss  $\leftarrow \frac{1}{n} \sum_{i=1}^n \alpha \times L_i$
  - 9: **end for**
  - 10: **Return:** loss
-



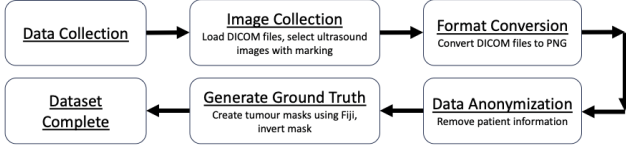


Figure 9. The steps involved in the creation of the US-TNBC dataset.

## E. Comparison with Transformer architectures

Table 3. Comparison with Transformer architectures. Scores are in %.

Model	TNBC		MonuSeg	
	Dice	IoU	Dice	IoU
TransUNet [14]	76.50	72.04	77.46	63.85
SwinUNet [8]	60.08	50.14	76.38	62.54
Ours	82.65	70.58	81.69	68.65

As seen in Table 3, the transformer architectures are data hungry models and are not suitable for data-scarce medical image segmentation tasks. We see that TransUNet and SwinUNet have lower Dice and IoU scores even with respect to the base UNet models (See Table 2). This shows that data-hungry Transformer architectures are not an ideal choice for medical domains with data scarcity.

## F. Significance testing

To rigorously evaluate the impact of the  $L_{fd}$ , we conducted a statistical significance test. The baseline model (for example, CMUNet without  $L_{fd}$ ) and five runs of the baseline model with  $L_{fd}$  was used for a one-sample t-test. It can be seen from Table 4 that  $p$ -values  $< 0.01$ , which makes the experiments statistically significant.

Model	Dice	IoU
<b>MoNuSeg</b>		
NuSegNet	0.0015	0.0032
AttnUNet	0.0019	0.0007
<b>US-TNBC</b>		
CMUNet	0.0045	0.0051

Table 4. Statistical significance ( $p$ -values).

## G. Details about the US-TNBC dataset

The TNBC dataset focuses on Triple-Negative Breast Cancer tissues. The images are typically 721 x 570 pixels in size on average. It consists of 30 images, including 15 ultrasound images and 15 ground truth images. The data collected at baseline includes breast ultrasound images of women aged between 42 and 76 years old. This data was collected between 2022 and 2023, and the images are in PNG format. To make the acquired data useful, some refinement tasks were performed. Firstly, the DICOM im-

ages were loaded into a DICOM reader, and the tumor images without marking or annotation were selected. Next, the DICOM files were converted into PNG format. The patient information was also eliminated using image cropping software. The images were cropped to retain maximum anatomical information while removing unnecessary boundaries and markers. The ground truth images were generated using Fiji, an open-source image processing program based on ImageJ2. The ground truth masks were produced and then inverted to match the UDIAT dataset mask convention, where the tumor masks are white and the background is black. This dataset is designed to evaluate algorithms for cancer detection, grading, and classification. The steps involved in the collection of the US-TNBC dataset are shown in Fig. 10. The dataset request link will be made accessible along with the code.

## H. Implementation details

We developed our segmentation model using Python and implemented it with the TensorFlow and Keras libraries. For data processing, we utilized numpy, OpenCV, and scikit-learn, enabling efficient data handling. We have used the high-performance NVIDIA TESLA P100 GPU to accelerate training and leverage hardware acceleration. The model has been trained for 100 epochs in the initial phase ( $\alpha = 0$ ) and 75 epochs in the second phase with  $L_{fd}$  ( $\alpha \neq 0$ ). It has been seen that this specific initialization of  $\alpha$  produces the best results as compared to other initialization values. This can be intuitively explained as the model learns to produce decent segmentation masks using the traditional  $L_{seg}$  and a regularization by  $L_{fd}$  utilizes the prior knowledge gained by the model in the 75 epochs to refine the feature maps. This effectively achieves a better Dice score (+1.5-1.9% across all datasets) than training the model with  $L_{fd}$  from the beginning. A train-test-validation split of 70-20-10% has been applied. Callbacks were used to save the best-performing model during both training phases. To address non-uniform image sizes, all images have been resized to uniform  $512 \times 512$  pixels for TNBC [50], the newly collected US-TNBC, and  $256 \times 256$  for UDIAT [75] and AD [32] (both  $256 \times 256$  and  $128 \times 128$ ). We have applied data augmentation (horizontal and vertical flipping, rotations to the left and right by  $90^\circ$ ) on the training set to train the models and on the test set to increase the number of data points for the plots. Evaluation of the models has been done on the test set without augmentation. Further details will be available with the code.

## I. Performance comparison on noisy input images

To evaluate model robustness under noisy conditions, Gaussian noise was systematically added to the images. For each

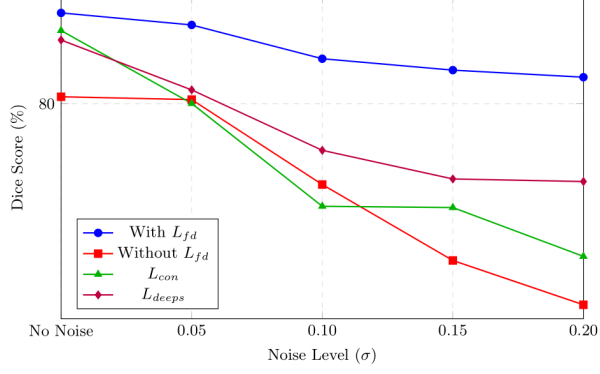


Figure 10. Analysis of the loss functions in the presence of noise added to input images while training. Dice score dips are less for  $\mathcal{L}_{fd}$  as compared to other losses as the strength of the noise increases.

image  $I \in \mathbb{R}^{H \times W \times C}$  in the dataset, zero-mean Gaussian noise  $\epsilon$  with standard deviation  $\sigma$  was sampled:

$$\epsilon \sim \mathcal{N}(0, \sigma^2) \quad (21)$$

The noisy image  $\tilde{I}$  was then computed as:

$$\tilde{I} = \text{clip}(I + \epsilon, 0, 1) \quad (22)$$

where  $\sigma$  was varied across experiments ( $\sigma \in \{0.05, 0.10, 0.15, 0.20\}$ ) and  $\text{clip}(\cdot)$  ensured valid pixel intensities. This process maintained original data dimensions while simulating realistic sensor noise artifacts. In this experiment, we see that the proposed  $\mathcal{L}_{fd}$  has lesser dip in the performance as compared to  $L_{con}$ ,  $L_{deeps}$  and  $L_{seg}$  (Without  $\mathcal{L}_{fd}$ , i.e., a combination of Dice loss and BCE loss). This indicates that foreground-background feature disentanglement ensures robust feature extraction even for noisy/poor-quality images.